Electronic and optical properties of ScN and (Sc,Mn)N thin films deposited by reactive DC-magnetron sputtering

Bivas Saha, Gururaj Naik, Vladimir P. Drachev, Alexandra Boltasseva, Ernesto E. Marinero, and Timothy D. Sands

Citation: Journal of Applied Physics **114**, 063519 (2013); doi: 10.1063/1.4817715
View online: http://dx.doi.org/10.1063/1.4817715
View Table of Contents: http://scitation.aip.org/content/aip/journal/jap/114/6?ver=pdfcov
Published by the AIP Publishing

Electronic and optical properties of ScN and (Sc,Mn)N thin films deposited by reactive DC-magnetron sputtering

Bivas Saha,[1,2] Gururaj Naik,[2,3] Vladimir P. Drachev,[2,3,4] Alexandra Boltasseva,[2,3]
Ernesto E. Marinero,[1] and Timothy D. Sands[1,2,3]
[1]*School of Materials Engineering, Purdue University, West Lafayette, Indiana 47907, USA*
[2]*Birck Nanotechnology Center, Purdue University, West Lafayette, Indiana 47907, USA*
[3]*School of Electrical and Computer Engineering, Purdue University, West Lafayette, Indiana 47907, USA*
[4]*Department of Physics, University of North Texas, Denton, Texas 76203, USA*

(Received 27 May 2013; accepted 16 July 2013; published online 14 August 2013)

Scandium nitride (ScN) is a rocksalt semiconductor that has attracted significant attention from various researchers for a diverse range of applications. Motivated by the prospect of using its interesting electronic structure for optoelectronic and dilute magnetic semiconductor applications, we present detailed studies of the electronic transport and optical properties of ScN and its alloys with manganese nitride (MnN). Our results suggest (a) dilute manganese doping in ScN compensates for the high *n*-type carrier concentrations arising due to oxygen impurities and (b) an *n*-type to *p*-type carrier type transition occurs at a composition between 5.8% and 11% Mn on Sc sites. In terms of its optical properties, our analysis clearly indicates direct and indirect bandgap absorption edges of ScN located at 2.04 eV and 1.18 eV, respectively. In addition to the direct gap absorption edge, (Sc,Mn)N samples also show Mn-defect induced electronic absorption. Photoluminescence measurements at room temperature from ScN films exhibit a yellowish-green emission corresponding to direct gap radiative recombination. Direct gap recombination is not expected given the smaller indirect gap. A possible role of high excitation intensities in suppressing relaxation and recombination across the indirect bandgap is suspected. Raman spectroscopic and ellipsometric characterization of the dielectric permittivities of ScN and (Sc,Mn)N are also presented to assist in understanding the potential of ScN for optoelectronic applications. [http://dx.doi.org/10.1063/1.4817715]

INTRODUCTION

Scandium nitride (ScN) is a non-tetrahedral indirect bandgap semiconductor[1,2] that has generated significant interest and is being explored by various researchers for its potential applications including thermoelectricity,[3–7] hot-carrier photovoltaic devices,[8] photonic metamaterials,[9] and others. Like most transition metal nitrides, ScN is mechanically hard, chemically stable, exhibits high corrosion resistance, and has an extraordinarily high melting temperature of 2600 °C. Currently efforts are also underway to grow high quality epitaxial superlattices and multilayers composed of rocksalt metal (ZrN, HfN, WN, and others) and ScN for their potential applications in thermionic energy conversion devices.[3,4] Recent theoretical proposals[10,11] have also indicated that Mn-doped ScN might exhibit dilute magnetic semiconducting properties having a Curie temperature in excess of 400 K. All of these developments in the theoretical understanding of the physical properties of ScN would be furthered with experimental investigations of the room temperature electronic and optical properties of ScN, connecting these results with its electronic structure. In this article, we present our detailed studies of the electronic transport characteristics and optical properties characterized by spectroscopic ellipsometry, absorption spectroscopy, photoluminescence, and Raman scattering of thin films of ScN and (Sc,Mn)N alloys[12] to understand their potential applications and suitability for optoelectronic devices.

In terms of its electronic properties, although ScN was long believed to be a semimetal,[13] recent modelling analysis from our group[1] and others[14–16] have suggested that ScN is an indirect bandgap semiconductor with a Γ-X indirect gap of 0.9 eV and a Γ-Γ direct gap of 2.2–2.7 eV. The high *n*-type carrier concentration of $\sim 1 \times 10^{20}$ cm^{-3} in typical films is due to the presence of defects,[17] nitrogen vacancies, and other impurities (usually oxygen). This high n-type carrier concentration is a challenge for electronic and optoelectronic device applications. Thus, reducing the concentration of unintentional donor dopants or defects combined with controlled introduction of acceptors will be necessary to fully realize the potential of ScN in devices. Manganese (Mn), being an electron acceptor in III–V nitrides, is a suitable choice for compensating donors and generating *p*-type material. Besides its potential for controlling the carrier concentration in ScN, its high solid solubility in rocksalt nitrides makes it ideal for exploring the possibility of a ScN-based dilute magnetic semiconductor.

In reference to optical properties, very little is known about ScN. As far as we have been able to verify, there are no reports of ScN's photoluminescence and spectroscopic dielectric properties in the UV-visible to near-IR range. Although there have been reports of properties such as optical reflection and transmission[18,19] in the visible to near-IR range, none of the reports describe the most salient feature of the optical properties of ScN, nor do they explain those properties in terms of its electronic structure. In this paper, we

first address the optical properties of ScN in employing the analysis of its electronic structure described in Ref. 1. Subsequently, we describe the optical properties of (Sc,Mn)N alloys.

The rocksalt crystal structure and octahedral bonding configuration of ScN make it ideal for alloying with Mn and other transition metals without precipitation or secondary phase formation. Yang *et al.*[12] have reported that the θ-phase of MnN has a face centered tetragonal crystal structure with a = b = 4.22 Å and c = 4.12 Å. MnN grown on (001) MgO using rf-plasma MBE in the temperature range of 250–450 °C exhibits (001) growth orientation and antiferromagnetic properties[20] at room temperature. The similar bonding and crystal structures of ScN and MnN have allowed us to grow homogeneous solid solution alloys of (Sc,Mn)N having a very high Mn concentration. In this article, however, we present the optical properties of (Sc,Mn)N films having Mn concentrations in the range of 0–11% on the Sc sites.

GROWTH OF (Sc,Mn)N FILMS

(Sc,Mn)N thin films were grown on (001) MgO substrates using reactive dc magnetron sputtering in a load-locked turbomolecular pumped high vacuum deposition system with a base pressure of 10^{-8} torr (PVD Products, Inc.). The growth chamber had the capability to accommodate four targets and was equipped with three dc power supplies. The Sc (99.998% purity) and Mn (99.99%) targets had dimensions of 2 in. diameter and 0.25 in. thickness. All depositions were performed with an Ar/N_2 mixture with the flow rates of Ar and N_2 being 2 and 8 sccm, which resulted in a sputter gas pressure of 5 mTorr. The targets were sputtered in constant power mode, and while the Sc target was fixed at 200 W, the Mn target power was varied from 5 to 20 Watts in order to achieve the desired Mn concentration in the films. The substrates were maintained at a temperature in the range of 500–750 °C during deposition, as determined using an infrared pyrometer operated in the wavelength range of 0.8–1.1 μm, together with a thermocouple.

Prior to the deposition of the films, MgO substrates with an off-cut between 0° to 1° were cleaned in ultrasonic baths of acetone and methanol to remove dust and to degrease, followed by blowing dry with N_2. The samples were then outgassed at 500 °C for 10 minutes in the vacuum chamber before deposition. MgO substrates were chosen because of their temperature stability, and the fact that they provide a satisfactory lattice match to the ScN layer having an in-plane lattice mismatch of 6.7%. The insulating behavior of MgO is also useful for measuring the electrical properties of the films.

STRUCTURE AND CHARACTERIZATION

All the (Sc,Mn)N films grow epitaxially on MgO substrates with (001) orientation as verified by high resolution X-ray diffraction (XRD) studies. The surface morphology as examined by scanning electron microscopy (SEM) suggests columnar growth. The symmetric 2θ-ω X-ray diffraction scan for a 3.8% MnN alloy sample is presented in Fig. 1. The inset shows four asymmetric φ-peaks that are separated by 90°, which confirms that the films grow epitaxially on the MgO substrates. The full-widths-at-half-maximum (FWHM) of the rocking curves of all of these films are in the range of 1°–1.5°, suggesting a modest degree of mosaicity despite the lattice mismatch with the substrate. The surface roughness of the films measured by atomic force microscopy (AFM) yielded an r.m.s roughness of approximately 0.56 nm for a ScN film and approximately 0.76 nm for a (Sc,Mn)N alloy film. The Mn concentrations in the films were determined by Rutherford Back-Scattering Spectrometry (RBS). High resolution transmission electron microscopy (HRTEM) combined with electron energy loss spectroscopy (EELS) analysis indicates the absence of any Mn secondary phase or of Mn clustering, thus suggesting a homogeneous uniform solid solution alloy. The details of the growth and microscopy characterization will be presented in a separate paper. Here, we limit our focus to the electrical and optical properties of the films.

One important point to note is that the ScN films prepared for this study were heavily *n*-type doped due to the presence of oxygen, attributed to the incorporation of oxygen from background residual water vapor, O_2, CO_2, and CO. RBS along with the nuclear reaction analysis (NRA) technique that provides improved sensitivity and accuracy in determining oxygen concentration (conducted by Evans Analytical Group (EAG)) suggests the presence of 1.6 ± 1.0

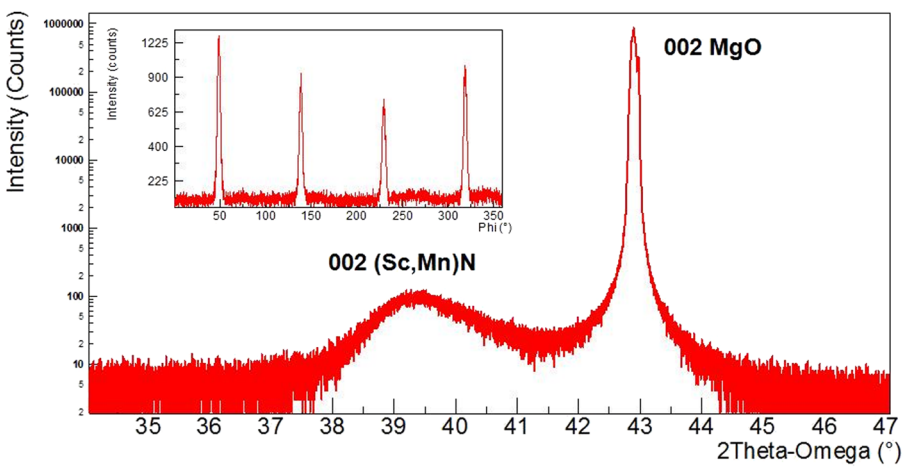

FIG. 1. Symmetric 2θ-ω X-ray diffraction spectrum of a (Sc,Mn)N alloy film with 3.8% MnN in the alloy sample grown on MgO substrate (in logarithmic scale). The spectrum indicates that the film grows with (001) orientation. The inset provides an asymmetric φ-scan of the same sample. Four equidistant φ-peaks are observed which suggest that the films are epitaxial on the MgO substrate.

atomic percentage of oxygen in a typical ScN film grown in the deposition system used for this study, a level that is expected to yield a carrier concentration (electrons) of about $10^{20}\,cm^{-3}$.

ELECTRICAL PROPERTIES

The electronic structure and the electron transport properties of ScN have been a subject of great interest for some time. Due to the large background carrier concentrations arising from impurities, experimental studies of the nature of the band structure of ScN have been inconclusive. The electronic structure of ScN previously calculated by a Density Functional Theory (DFT)-based approach[1] is reproduced in Fig. 2(a) to aid in explaining the electronic and optical properties. Since the ScN films grown for the present study contain oxygen impurities, we have also performed DFT calculations to understand the effect of oxygen on the electronic properties of ScN. Details of these calculations and the results are presented in Ref. 7. A brief description of the electronic structure of oxygen-doped ScN is provided here to assist in interpreting the electrical and optical properties of ScN and (Sc,Mn)N films. Our analysis has established that (a) oxygen in ScN mixes uniformly on the N site, forming a homogeneous solid-solution alloy, (b) in terms of its electronic structure; oxygen impurities in ScN shift the Fermi energy from inside the bandgap into the conduction band without appreciably altering the basic band structure and the densities of states. For 1.6 ± 1 atomic percent oxygen in ScN films, our calculations suggest that the Fermi energy is about 0.08–0.34 eV above the conduction band edge.

Based on this understanding of the electronic structure, we explain the electrical properties of ScN and (Sc,Mn)N films. The room temperature in-plane resistivity, mobility and carrier concentration of these films were measured using a Hall effect system in the Van der Pauw geometry on ~300 nm thick films that were grown on 1 cm × 1 cm MgO substrates. Fig. 3 represents the electrical resistivity and carrier concentration as a function of Mn concentration in ScN films and indicates that ScN has an electrical resistivity of 2 mΩ-cm and a carrier concentration of $10^{20}\,cm^{-3}$. Since the

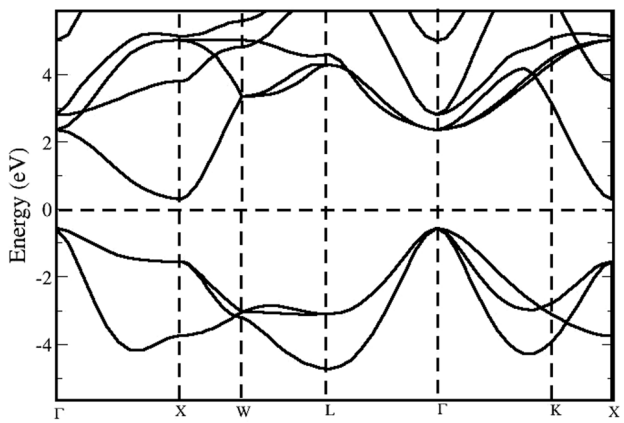

FIG. 2. Electronic structure of ScN along the high symmetry directions of the Brillouin zone, calculated by density functional theory. Reproduced with permission from B. Saha et. al., J. Appl. Phys. 107, 033715 (2010). Copyright 2010 American Institute of Physics.

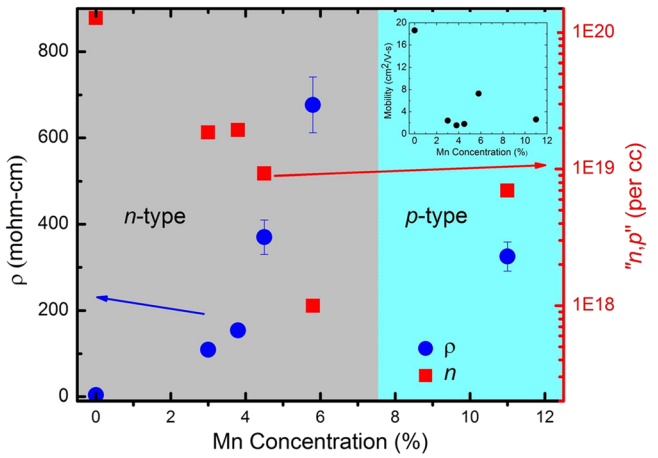

FIG. 3. Electrical resistivity and carrier concentration as a function of Mn concentration in (Sc,Mn)N films. A noteworthy *n*-type to *p*-type carrier transition is observed around 5.6% MnN in the (Sc,Mn)N matrix. We measured the resistivity of the samples with four-point probe method also and the error bar indicates the uncertainty in measurement when we employ two different approaches (namely the four-point probe method and van-der pauw method). The inset represents the mobility of the ScN and (Sc,Mn)N alloy films as a function of Mn concentration.

measured atomic concentration of oxygen in the ScN films is 1.6 ± 1.0 at. %, this would imply that the measured carrier concentration can be attributed to oxygen donor doping. Fig. 3 also indicates that as Mn is incorporated in ScN films, the resistivity increases and the carrier concentration drops. The resistivity peaks between 5.8% and 11% MnN in the (Sc,Mn)N alloy, beyond which the alloy becomes *p*-type.

The behavior of the electrical resistivity as a function of the Mn concentration can be explained through our understanding of the electronic structure of ScN with oxygen impurities. Mn in ScN acts as an electron acceptor and compensates for the extra electrons arising due to oxygen impurities. As the Mn concentration is increased in ScN, the carrier concentration in the film decreases (see Fig. 3) and the Fermi level moves from the conduction band into the bandgap, which results in an increase of the resistivity. With the increase in Mn concentration, a special situation arises when the Fermi level resides in the middle of the gap resulting in the peak of the resistivity at a %MnN between 5.8% and 11%. For higher Mn concentrations, the sample becomes *p*-type as the Fermi energy approaches the valence band, resulting in a decrease in the resistivity. The carrier concentration at the compensation point is lower than $1 \times 10^{18}\,cm^{-3}$ suggesting that intrinsic ScN should have a carrier concentration below $10^{18}\,cm^{-3}$, and the extra $10^{20}\,cm^{-3}$ carriers originate from oxygen impurities.

The mobilities of the ScN and (Sc,Mn)N alloy samples are presented in the inset of Fig. 3. Pure ScN films have a mobility of 18.6 cm^2/Vs at room temperature. Previously we have reported (see Ref. 7) a very high mobility of 106 cm^2/Vs for the sputter deposited ScN films, and the lower values of mobility presented here are due to the difference in the growth conditions and growth temperature. Fig. 3 also suggests that as MnN is added into the ScN matrix, the mobility decreases, which is consistent with an impurity scattering mechanism. However, mobility starts to increase as the *n*-type to *p*-type

carrier transition regime is approached and becomes maximum at 5.8% MnN in the (Sc,Mn)N matrix. The *p*-type (Sc,Mn)N alloy that has 11% MnN in (Sc,Mn)N, however, has a very low mobility of 2.6 cm^2/Vs.

Thus, Mn doping in ScN provides a lever to control its electrical properties. The high carrier concentrations and high conductivity that results from the oxygen impurities in ScN can be compensated by the introduction of acceptor-like Mn atoms on Sc sites.

OPTICAL PROPERTIES

Absorption studies

In order to understand optical properties such as the bandgap and the energy of the predominant Mn defect states as a function of the concentration of Mn dopant, we measured the transmission (T) and reflection (R) spectra of the samples from the UV to the near-IR-range (320 nm to 1100 nm). Since MgO is transparent in the spectral region of our interest, all of these measurements were performed on films grown on MgO substrates. The substrates were single-side polished, and thus, transmittance measurements were made using an integrating sphere configuration. A Lambda 950 UV-Vis-NIR spectrometer (PerkinElmer) with an integrating sphere was used to measure the reflection and transmission. The spectroscopic data were collected with a wavelength step of 10 nm.

The absorption (A) spectra (calculated using the measured R and T and presented in Fig. 4(a)) give us insights into the optical transitions taking place in ScN and its alloys with MnN. Two distinct transitions can be observed in Fig. 4(a) suggesting that ScN has a direct gap absorption edge (at the Γ-point of the Brillouin zone) around 570 nm. A smaller absorption peak at ~735 nm is observed and is attributed to the electronic transitions from the Γ-X region of the valence band to the corresponding regions in the conduction band of the Brillouin zone. Above the direct gap edge, the absorption saturates, while in the long wavelength limit the absorption tails off. Similar direct bandgap absorption edges have been observed in ScN samples grown with rf-MBE.[18] The absorption spectra of the (Sc,Mn)N samples also exhibit direct gap edges similar to pure ScN; however, they are red shifted. The degree of the shift increases with the Mn concentration. These alloy samples also show spectral features indicative of defect states, with an absorption peak in the red to near-IR part of the spectrum whose position shifts to longer wavelengths as the Mn concentration is increased.

In order to understand the origin of these absorption spectra and to quantify the absorption band edges and defect states, the absorption coefficients (α_{abs}) for the interband transitions were calculated using the Beer-Lambert law from the absorption data. Since, for semiconductors with parabolic electronic bands, the absorption coefficient (α_{abs}) varies with the photon energy as[21] $\alpha_{abs} \sim \frac{(\hbar\omega - E_g)^{\frac{1}{2}}}{\hbar\omega}$, we plot $(\alpha\hbar\omega)^2$ as a function of the photon energy in Fig. 4(b) and extract the direct bandgap (E_g). The values of the direct gap are presented in Fig. 4(c) as a function of the Mn concentration. Our results suggest that ScN has a direct gap of 2.03 eV consistent with the known value of its bandgap in the literature.[18] This direct gap absorption edge results from the electronic transition at the Γ-point of the Brillouin zone, which was overestimated to be located at 2.3–2.7 eV in our electronic structure calculations of ScN (see Fig. 2(a) and Ref. 1). Fig. 4(c) also suggests that this direct gap shrinks as Mn is incorporated in the films, while the bandgap values saturate above 5.8% MnN in the alloy. The electronic density of states of a 6.25% MnN alloy was calculated using DFT and is presented in Fig. 4(d). The results of Fig. 4(d) suggest that Mn doping in ScN introduces impurity states just above the valence band edge, effectively reducing the valence to conduction band energy difference.

Besides the direct gap absorption described above, another absorption peak in Fig. 4(b) for ScN is evident at 1.7 eV. The origin of this absorption peak can be explained through our understanding of the electronic structure of ScN and its joint density of states. The joint density of states ($\rho_{cv}(\hbar\omega)$) is the number of states per unit volume per unit energy range which occur with an energy difference between the conduction and the valence bands and is given by the following expression:[21]

$$\rho_{cv}(\hbar\omega) = \frac{2}{8\pi^3}\iint \frac{ds}{|\nabla_k\ (E_c - E_v)|_{E_c - E_v = \hbar\omega}}.$$

It suggests that in those regions in the Brillouin zone where $(E_c - E_v)$ is constant and has the value of $\hbar\omega$, $\nabla_k\ (E_c - E_v)$ is small and the probability of the inter-band transitions is a maximum. Careful observation of the electronic structure of ScN (see Fig. 2(a)) indicates that the energy difference $(E_c - E_v)$ has a relatively low gradient or is nearly constant at 1.75 eV as one moves away from the X(100) point towards the Γ-point. This result in a large probability for interband transitions around this photon energy as the joint densities of states is very high around these regions of the Brillouin zone. The absorption peak at 1.76 eV may result directly from these transitions. A similar behavior has been observed in another indirect bandgap material, namely, germanium.[21] The energy difference $(E_c\text{-}E_v)$ at L points in Ge has a relatively small gradient as one moves away from the L point, and therefore, the interband transitions were reported to be much stronger at the corresponding energy.

In the (Sc,Mn)N samples, the absorption peaks in the low energy part of the spectrum are primarily dominated by the absorption of Mn mid-gap defect states. The peak of these absorption red-shifts as the Mn concentration in the ScN films is increased. This implies that the defect states move closer to the valence band edge as increasing amounts of Mn are incorporated into the ScN films (see Fig. 4(c)). It is noted that the energy difference between the direct band absorption peak and the mid-gap absorption peak remains nearly constant at around 0.5 eV for all the (Sc,Mn)N alloy samples. Also, the absorption peak at lower energy becomes stronger for larger Mn concentrations. This suggests that Mn introduces mid-gap defect states that are responsible for the absorption at lower photon energies. The electronic transitions from the acceptor states to the conduction band edge are responsible for the absorption

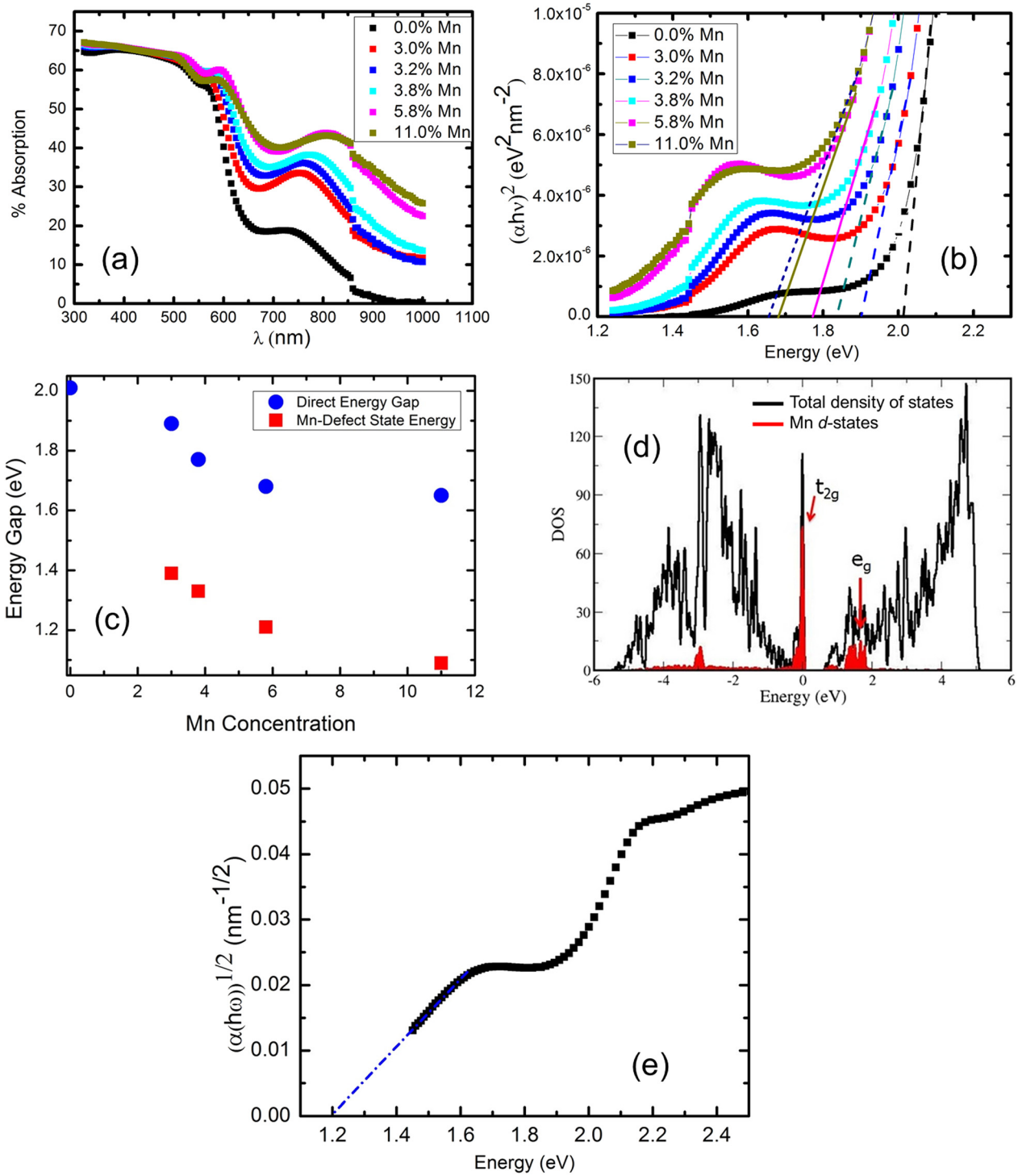

FIG. 4. (a) Absorbance spectra, (b) absorption coefficient of ScN and (Sc,Mn)N alloy films having different Mn concentrations. Apart from the direct bandgap absorption edge, Mn defect induced absorption is observed in the (Sc,Mn)N films. (c) The direct energy gap and the Mn-defect state energy as a function of Mn concentrations. The energy separation of these two different absorption peaks is constant with varying Mn concentration. (d) Electronic density of states of 6.25% MnN in a (Sc,Mn)N alloy calculated within the density functional theory. (e) Square-root of the absorption coefficient plot as a function of the photon energy and extraction of the indirect bandgap. The curve has a discontinuity at 1.44 eV due to the change in photon source at this particular energy.

peak at around 720–830 nm. The mid-gap absorption arises from electronic transitions between acceptor states near the valence band edge and the mid-gap defect states. As the Mn concentration is increased, the edge of the acceptor band moves up into the gap, thus reducing the photon energy corresponding to the peaks of both the bandgap and the mid-gap absorption bands by the same amount. This explains why the energy difference between the absorption peaks remains constant with varying Mn concentration. The origin of the mid-band defect states may be attributed to two plausible mechanisms: (1) Mn *d*-orbitals in the octahedral environment of the nitrogen ligands split into the t_{2g} and e_g bands due to octahedral distortion, or (2) the Mn in the ScN films might have two different oxidation states, e.g., Mn^{4+} and Mn^{3+}. Our electronic

structure calculations of (Sc,Mn)N (see the density of states of an alloy with 6.25% MnN in Fig. 4(c)) suggest that the t_{2g} and e_g bands of Mn *d*-states does split inside the direct bandgap of the semiconductor, with the peaks of the t_{2g}^3 states lying at the Fermi energy and spreading over the Fermi edge near the valence band, and the e_g^2 states located near the conduction band. This explains why we see a constant energy difference between the direct gap and the Mn defect states.

An estimate of the indirect bandgap of ScN is very difficult due to the small absorption cross-section for the indirect bandgap edge. Our task is further complicated by the fact that the ScN films contain oxygen atoms as impurity. As we have mentioned before, the Fermi energy of ScN is inside the conduction band by 0.08–0.34 eV above the band edge, the absorption edge is expected to be blue shifted, corresponding to the Moss-Burstein shift of a highly doped semiconductor. The optical absorption in an indirect bandgap material is expressed[21] by the relation $\alpha_{abs}(\hbar\omega) \sim (\hbar\omega - Eg \pm \hbar\omega_q)^2$, where $\hbar\omega_q$ is the energy of the phonon absorbed or emitted. Thus, we plot the square root of the absorption coefficient in Fig. 4(e). The plot indicates a clear indirect absorption edge that intercepts the energy axis at ~1.2 eV. As our modelling results indicate that the level of oxygen impurity in the films would shift the Fermi energy by 0.08–0.34 eV above the conduction band edge, we conclude that undoped ScN thin films have an indirect energy gap of around 0.9–1.0 eV consistent with our DFT calculations[1] (see Fig. 2(a)).

PHOTOLUMINESCENCE AND RAMAN SPECTROSCOPY

Photoluminescence (PL) studies of degenerate or doped semiconductors yield information that is important for the understanding of electronic properties, band alignment, nature of the defect states, and other optoelectronic properties.[22–24] Direct gap luminescence from an indirect gap material is improbable as the excited electrons in the conduction band thermalize rapidly to the indirect conduction band minima. However, there are many reports of radiative recombination or PL across direct bandgaps in otherwise indirect gap semiconductors such as Ge.[25,26] We next discuss the direct bandgap room temperature PL properties of ScN. We show how the observed luminescence is quenched with the introduction of Mn into the ScN films.

A T-64000 Raman spectrometer equipped with a liquid nitrogen cooled detector was employed to study photoluminescence and Raman spectroscopic properties of ScN. An Ar-Kr laser having an excitation wavelength of 488 nm was used as the pump source. We also conducted measurements with the 480 nm emission line of the Ar-Kr laser. PL spectra

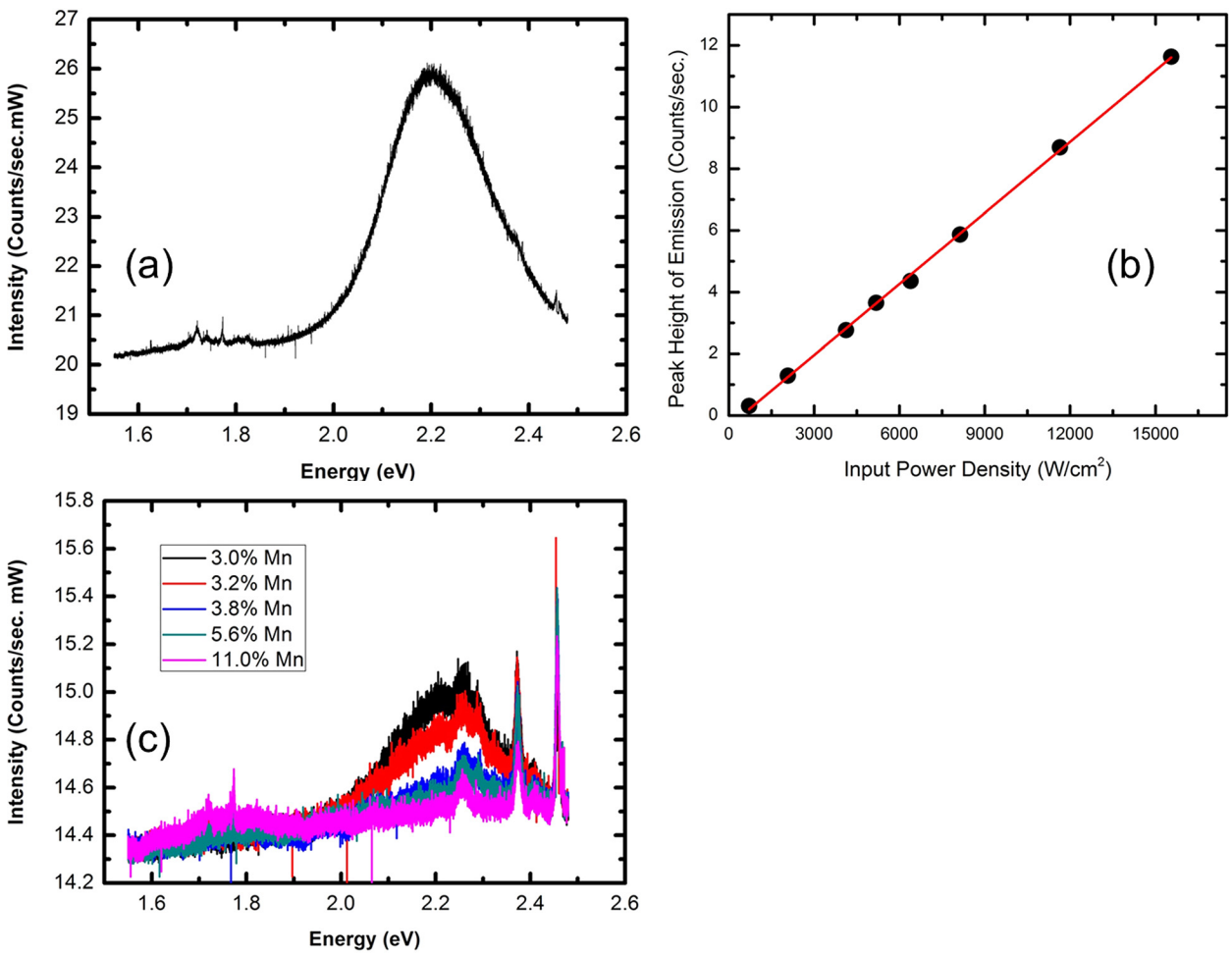

FIG. 5. (a) Photoluminescence spectra of ScN at room temperature. (b) Peak height of the PL vs input laser power density. (c) PL of (Sc,Mn)N films. Luminescence is strongly quenched with the incorporation of Mn.

were collected from 500 nm to 800 nm with 10 nm spectral resolution.

The PL spectrum of a ScN thin film is presented in Fig. 5(a), exhibiting a maximum at 557 nm that arises from the direct bandgap excitation of the semiconductor. The full-width-at-half-maximum (FWHM) of the luminescence peak is about 0.25 eV which is much broader than peaks from conventional direct bandgap semiconductors such as ZnO[27] or GaN,[28] where the FWHM from direct gap emission is in the range of 0.02–0.05 eV, but nevertheless comparable with the direct gap radiative recombination peak of Ge.[25] A change in the excitation wavelength from 488 nm to 480 nm does not change the peak position of the emission. The peak height, however, changes a little due to the variations in the input laser power hitting the sample. Very small emission features are observed in the spectral region from 680 to 730 nm that arise from defect states in the substrate (MgO) as observed from the PL of our bare MgO substrates.

Several mechanisms ranging from the presence of defect states, the nature of the band structure, heavy dopant concentrations, and high excitation intensity have been proposed for direct gap radiative recombination in indirect bandgap semiconductors.[26] In fact, band-structure engineering with both *n*-type and *p*-type doping in germanium[25,26] has been successfully used to observe direct gap emission. Direct gap emission from undoped germanium samples has also been reported by several groups due to high optical excitation levels.[29,30] Intense optical excitation creates holes in the valence band and electrons in the conduction band which gives rise to direct gap emission for germanium without any dopant or impurity involved. In pure germanium one would require an intense optical excitation[30] of 1 kW/cm^2 to achieve such luminescence.

In our studies of the photoluminescence of ScN, we find that a threshold power density of 660 W/cm^2 is required to observe the direct gap luminescence. Under these high power densities (greater than 660 W/cm^2), holes (minority carriers) are created in the valence band while electrons (majority carriers) are photogenerated in the conduction band. The rate of radiative recombination (r_{sp}) is given by the expression

$$r_{sp} = \frac{8\pi n_s^2}{h^3 c^2} \frac{\alpha(E) E^2}{e^{\frac{E-\Delta\mu}{KT}} - 1},$$

where $\alpha(E)$ is the absorption coefficient, E is the energy which is released during the emission, n_s is the refraction index of the surface, $\Delta\mu = E_{Fn} - E_{Fp}$ is the energy difference between the quasi-Fermi levels under quasi-equilibrium condition, h and c are Plank's constant and the velocity of the light, respectively. Although the population of electrons in the indirect gap valley at the X point of the Brillouin zone is greater than that of the Γ-valley due to thermalization of the electrons (which typically is a fast process with a characteristic time of ∼100ps), the radiative recombination rate for the Γ_c-Γ_ν transition is very fast, and under high carrier populations owing to large excitation intensity, it is very much possible to observe the direct gap luminescence. For excitation intensity less than 660 W/cm^2, there are not enough electrons in the direct gap Γ valley to give sufficient luminescence, or whatever little emission that takes place is absorbed by the solid. The recombination rate also suggests that since the absorption coefficient for the indirect gap transition is very small (see Optical Properties section), coupled with the extra requirement of phonon participation due to momentum conservation; the radiative recombination across the indirect gap will be extremely small. However, we cannot verify this indirect gap emission as our detector does not allow detection of photons beyond the 900 nm spectral range.

In order to further verify the above explanation for photoluminescence in ScN, we varied the laser power (0.56–12.21 mW) using neutral density filters and recorded the PL spectra by focusing the output power down to a spot size of 10 μm radius on the sample. The results of Fig. 5(b) show that the amplitude of the PL at its peak value decreases linearly as the input power is reduced above the threshold power density required for photoemission. Such linear behavior in photoluminescence is expected as increasing the input power density linearly increases the hole (minority carrier) concentration in the valence band, while the increase in the electron concentration is negligible compared to the high background electron concentration. Similar linear dependence of the luminescence intensity on the incident laser power is observed in case of direct gap radiative recombination for *p*-type Ge.[26]

The luminescence spectra for the (Sc,Mn)N samples as shown in Fig. 5(c) indicate that the introduction of Mn in the ScN films quenches the photoluminescence, with the peak of the PL decreasing in intensity with increasing Mn concentration. The observed quenching of the luminescence can be explained by a trap-assisted non-radiative decay mechanism through our understanding of the electronic structure of (Sc,Mn)N. The Mn defect states near the valence and conduction bands trap the excited electrons and act as non-radiative decay paths for the excited electrons, thereby reducing the luminescence intensity with increasing Mn-concentration.

To understand the vibrational properties of these materials, Raman spectra of ScN and (Sc,Mn)N alloy samples (see Fig. 6(a)) were also measured and are explained with the aid of the calculated vibrational spectra of ScN[1] (see Fig. 6(b)). As mentioned earlier, ScN has a rocksalt crystal structure, with an octahedral bonding configuration. The theory of Raman scattering suggests that due to symmetry restrictions, the first-order Raman signal should be absent in such a rocksalt crystal structure. However, the presence of defects in the structure lifts the restriction of the *q*-selection rules, giving rise to second-order Raman peaks. Thus, the strong Raman lines in ScN and (Sc,Mn)N films can be attributed to the defect-induced second-order scattering mechanism.

The Raman spectroscopic measurements were carried out using a laser source with wavelength of 532 nm. The most intense Raman line in ScN is measured at ∼677 cm^{-1} and has a peak position comparable with the measurement of 676 cm^{-1} by Gravalnini *et al.*[19] Careful comparison of this Raman line with the DFT based modelling of the vibrational spectra of ScN (adapted from our previous work and presented in Fig. 7(b)) suggests that the Raman line at 677 cm^{-1} originates from transverse optical (TO) phonon modes. The measured Raman line, however, is softer by 50 cm^{-1} with

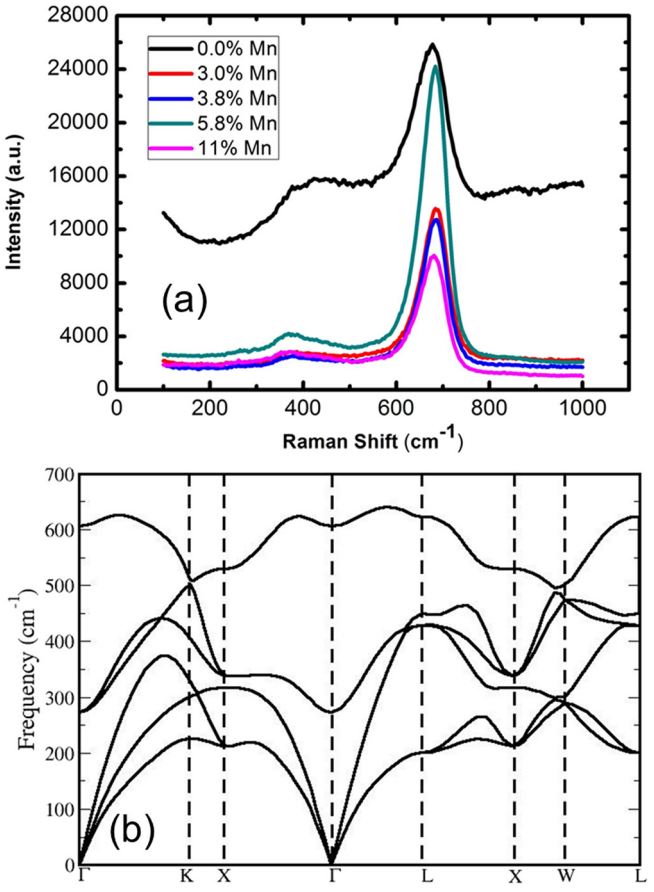

FIG. 6. (a) Raman spectra of ScN and MnN alloyed ScN films. The second-order defect-induced Raman peaks primarily arise from longitudinal optical (LO) phonons. (b) Vibrational spectrum of ScN calculated using Density Functional Theory (DFT). Reproduced with permission from B. Saha et. al., J. Appl. Phys. **107**, 033715 (2010). Copyright 2010 American Institute of Physics.

respect to the calculated values. Modelling results also suggest that the TO mode vibrations observed here is primarily an N-N vibrational state. The FWHM of this peak is 80 cm^{-1}. Acoustic modes that are primarily dominated by the vibration of Sc atoms have a relatively weak signature in the Raman spectra. Although there is no distinct peak in the Raman spectra for these acoustic phonon modes, a broad feature centred at 450 cm^{-1} is observed.

The Raman spectra for the (Sc,Mn)N samples (presented in Fig. 6(a)) suggest a similar TO phonon mode as in ScN. The peak positions of this vibrational mode shift only slightly with increasing Mn concentration. Since the lattice constant of the (Sc,Mn)N films varies only slightly with the Mn concentration, such slight increases in the vibrational frequency are not surprising. The peak height of the main TO Raman line also increases with increments in the Mn concentration. Since higher Mn concentrations in ScN result in more defect states and distortions of the lattice structure, the increase in the peak height is a manifestation of the defect-induced second-order Raman spectra. The FWHMs of these peaks are in the range of 65–70 cm^{-1}. The (Sc,Mn)N samples also show very little signature of their acoustic vibrational modes in the Raman spectra as these are defect-induced second-order Raman spectra.

ELLIPSOMETRY CHARACTERIZATION

To understand ScN's suitability as a dielectric component in the visible to near IR wavelength range, the dielectric permittivity of ScN and (Sc,Mn)N were measured using spectroscopic ellipsometry in the wavelength range of 300–2000 nm. Although Travglini *et al.*[19] have reported dielectric characteristics of ScN in the deep UV-range, there exists little understanding of the optical parameters in the visible to near IR-range and on the optical processes that govern these dielectric properties. A combination of Drude, Lorentz, and Tauc-Lorentz models[21] was used to retrieve the dielectric functions of the films. While the Drude model takes care of the free-electron response primarily in the near IR range, Lorentz and Tauc-Lorentz peaks are used to fit the interband transitions in the visible part of the spectrum. However, we cannot observe the electronic transitions due to the defect states since we have performed all the ellipsometry measurements in the reflection mode where the relevant information from defect is masked by interference effects.

In Fig. 7(a), the real (ϵ') and imaginary (ϵ'') parts of the dielectric permittivity are plotted, which suggest that ScN behaves as a dielectric in the visible to near-IR wavelength range. The real part of the dielectric constant at the interband transition position is large, having a value of 12.8, which is consistent with our calculated value of $\epsilon(\infty) = 12.3$[1]. The imaginary part of the dielectric constant which represents optical losses shows a peak in ϵ'' at 530 nm corresponding to the interband transition at the direct gap. In Fig. 7(a), we show also the Drude and the non-Drude contributions to the permittivity. The graph indicates that in the near IR-range, ϵ' decreases, whereas ϵ'' increases and this is due to free electron absorption or Drude contributions. Since ScN is a degenerate semiconductor having a very high carrier concentration of $\sim 10^{20}$ cm^{-3}, Drude losses associated with free carrier absorption are expected. The non-Drude part is primarily characterized by Lorentz peaks that describe the interband transition in ScN. While the Lorentz peak located at 530 nm is indicative of the direct gap transition, the Lorentz peak shown at 400 nm is above the direct gap and does not provide any new information.

The (Sc,Mn)N films were also characterized by ellipsometry based measurements, and our analysis (see Fig. 7(b)) indicates that the real part of the dielectric permittivity of the (Sc,Mn)N alloy samples behaves in a similar way as in ScN in the visible range. In the near IR-range, however, the free-carrier-induced Drude response is significantly different for these Mn doped samples when compared to the ScN Drude response. Since the introduction of Mn in ScN reduces its carrier concentration, the Drude contribution to the permittivity decreases with increasing Mn concentration. This manifests itself by a constant value of ε' in the near IR–range. The optical losses also decrease in these (Sc,Mn)N samples in the near IR range.

CONCLUSION

In conclusion, we have presented extensive experimental analysis of the electronic transport and optical properties

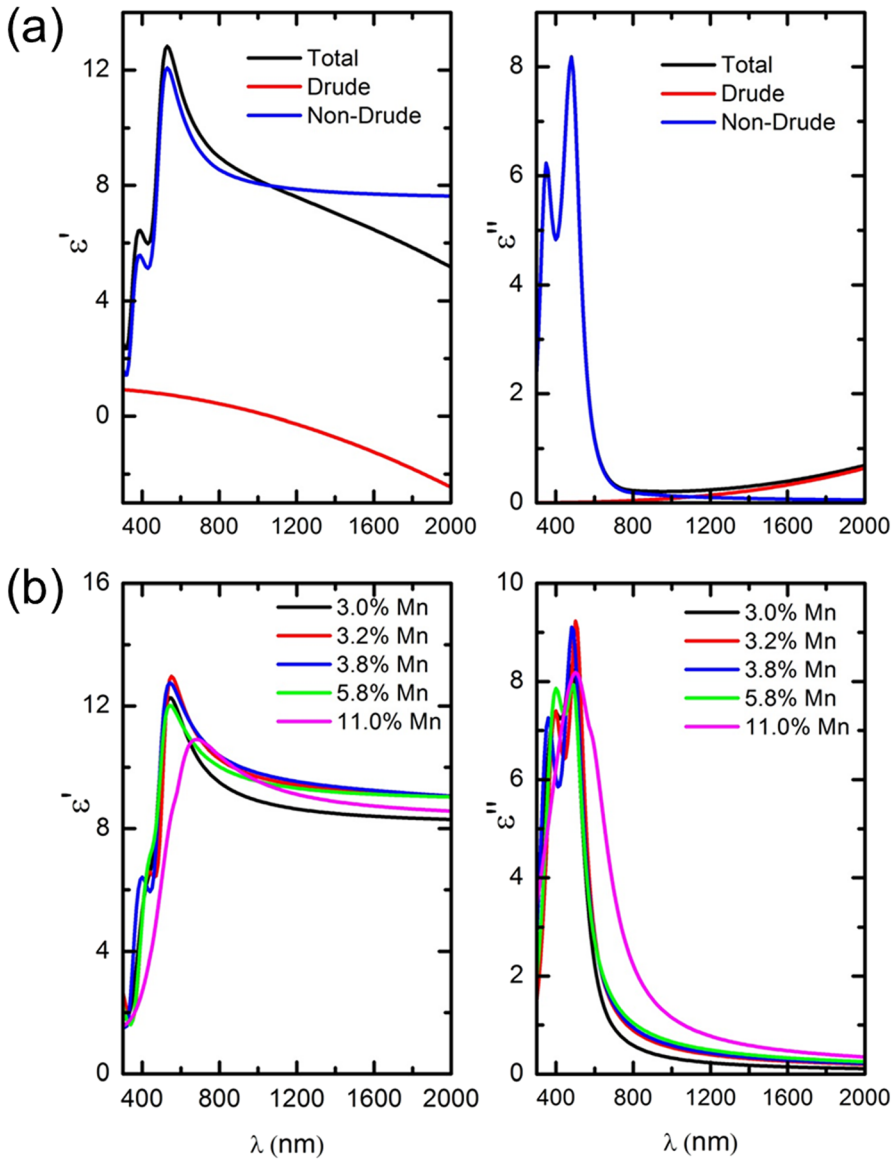

FIG. 7. (a) Real and Imaginary components of the dielectric permittivity of ScN. The Drude part and the non-Drude contribution are plotted together with the total permittivity. (b) Real and imaginary part of the permittivity of the (Sc,Mn)N samples.

of ScN and its alloys with MnN. These results are explained through theoretical calculations based on density functional theory. The large carrier concentration and high electrical conductivity in ScN that results from oxygen impurities are compensated by the introduction of manganese which acts as an electron acceptor in ScN. An interesting *n*-type to *p*-type carrier transition is observed in this system, which opens up the range of device possibilities for ScN. The optical studies comprising absorption, PL, Raman, and spectroscopic ellipsometry provide insights into the physical origin of the optical properties of this rocksalt semiconductor and its alloys with MnN. The absorption studies indicate direct, indirect, and Mn-induced defect gap absorption edges, all of which were explained by our understanding of the electronic structure of ScN and (Sc,Mn)N. To fully realize the potential of ScN-based heterostructures in electronic and optoelectronic devices, it will be necessary to substantially reduce the oxygen impurity concentration, to control native point defects (especially N vacancies) and to develop heterostructures with tunable band lineups. The chemical and thermal stability of ScN, along with the broad range of heterostructures possible in the rocksalt nitride materials system, justify further pursuit of fundamental understanding of ScN, its alloys and heterostructures for future applications in useful devices.

ACKNOWLEDGMENTS

B.S. and T.D.S. thank NSF/DOE-Thermoelectrics Partnership: Purdue—GM Partnership on Thermoelectrics for Automotive Waste Heat Recovery program for funding this research, G.N. and A.B. thank support from ARO (grant 57981-PH (W911NF-11-1-0359)) and NSF (MRSEC grant DMR-1120923), and V.P.D. thanks a partial support by AFRL Materials and Manufacturing Directorate - Applied Metamaterials Program.

[1]B. Saha, J. Acharya, T. D. Sands, and U. V. Waghmare, J. Appl. Phys. **107**, 033715 (2010).
[2]D. Gall, M. Stadele, K. Jarrendahl, I. Petrov, P. Desjardins, R. T. Haasch, T.-Y. Lee, and J. E. Greene, Phys. Rev. B **63**, 125119 (2001).
[3]M. Zebarjadi, Z. Bian, R. Singh, A. Shakourie, R. Wortman, V. Rawat, and T. Sands, J. Electron. Mater. **38**, 960 (2009).
[4]V. Rawat, Y. Koh, D. Cahill, and T. Sands, J. Appl. Phys. **105**, 024909 (2009).

[5]B. Saha, T. D. Sands, and U. V. Waghmare, J. Appl. Phys. **109**, 083717 (2011).
[6]B. Saha, T. D. Sands, and U. V. Waghmare, J. Phys. Condens. Matter. **24**, 415303 (2012).
[7]P. Burmistrova, J. Maassen, T. Favaloro, B. Saha, S. Salamat, Yee Rui Koh, M. Lundstrom, A. Shakouri, and T. D. Sands, J. Appl. Phys. **113**, 153704 (2013).
[8]G. Conibeer, Mater. Today **10**, 42–50 (2007).
[9]G. V. Naik, B. Saha, T. D. Sands, and A. Boltasseva, in 4th International Topical Meeting on Nanophotonics and Metamaterials (NANOMETA 2013), Seefeld, Austria, 2-6 January, 2013.
[10]A. Herwadkar and W. R. L. Lambrecht, Phys. Rev. B. **72**, 235207 (2005).
[11]A. Herwadkar, W. R. L. Lambrecht, and M. V. Schilfgaarde, Phys. Rev. B **77**, 134433 (2008).
[12]In this manuscript, we refer to (Sc,Mn)N alloys, recognizing that the N-rich Mn-N phase is likely deficient in N relative to the ideal 1:1 stoichiometry. (a) H. Yang, H. Al-Brithen, E. Trifan, D. C. Ingram, and A. Smith, J. Appl. Phys. **91**, 1053 (2002); (b) F. Lihl, P. Ettmayer, and A. Kutzelnigg, Z. Metallkd. **53**, 715 (1962).
[13]A. Neckel, P. Rastl, R. Eibler, P. Weinherger, and K. Schwartz, J. Phys. C: Solid State Phys. **9**, 579 (1975).
[14]C. Stampfl, W. Mannstadt, R. Asahi, and A. J. Freeman, Phys. Rev. B. **63**, 155106 (2001).
[15]W. R. L. Lambrecht, Phys. Rev. B **62**, 13538 (2000).
[16]A. Qteish, P. Rinke, M. Scheffler, and J. Neugebauer, Phys. Rev. B **74**, 245208 (2006).
[17]M. A. Moram, Z. H. Barber, and C. J. Humphreys, Thin Solid Films **516**, 8569–8572 (2008).
[18]A. R. Smith, H. A. H. AL-Brithen, D. C. Ingram, and D. Gall, J. Appl. Phys. **90**, 1809 (2001).
[19]G. Travaglini, F. Marabelli, R. Monnier, E. Kaldis, and P. Wachter, Phys. Rev. B **34**, 3876 (1986).
[20]H. A. Al-Brithen, H. Yang, and A. R. Smith, J. Appl. Phys. **96**, 3787 (2004).
[21]M. S. Dresselhaus, Solid State Physics, Part II, Optical Properties of Solids; MIT Solid State Physics Course. 2001.
[22]K. Vanheusden, W. L. Warren, C. H. Seager, D. R. Tallant, and J. A. Voigt, J. Appl. Phys. **79**, 7983 (1996).
[23]F. L. Singh, F. L. J. Molnar, M. S. Ii, and T. D. Moustakas, Appl. Phys. Lett. **64**, 336 (1994).
[24]Y. Zhang, B. Fluegel, A. Mascarenhas, H. P. Xin, and C. W. Tu, Phys. Rev. B. **62**, 4493, (2000).
[25]M. El Kurdi, T. Kociniewski, T.-P. Ngo, J. Boulmer, D. Débarre, P. Boucaud, J. F. Damlencourt, O. Kermarrec, and D. Bensahel, Appl. Phys. Lett. **94**, 191107 (2009).
[26]J. Wagner and L. Vina, Phys. Rev. B. **30**, 7030 (1984).
[27]S. Cho, J. Ma, Y. Kim, Y. Sun, G. K. L. Wong, and J. B. Ketterson, Appl. Phys. Lett. **75**, 2761 (1999).
[28]W. Grieshaber, E. F. Schubert, I. D. Goepfert, R. F. Karlicek, Jr., M. J. Schurman, and C. Tran, J. Appl. Phys. **80**, 4615 (1996).
[29]H. M. Van Driel, A. Elci, J. S. Bessay, and M. O. Scully, Solid State Commun. **20**, 837 (1976).
[30]W. Klingenstein and H. Schweizer, Solid State Electron. **21**, 1371 (1978).